Experiments in Fluids 29 (2000) 339–346 © Springer-Verlag 2000

Simultaneous density-field visualization and PIV of a shock-accelerated gas curtain

K. Prestridge, P. M. Rightley, P. Vorobieff, R. F. Benjamin, N. A. Kurnit

Abstract We describe a highly-detailed experimental characterization of the Richtmyer-Meshkov instability (the impulsively driven Rayleigh-Taylor instability) (Meshkov 1969; Richtmyer 1960). In our experiment, a vertical curtain of heavy gas (SF_6) flows into the test section of an air-filled, horizontal shock tube. The instability evolves after a Mach 1.2 shock passes through the curtain. For visualization, we pre-mix the SF_6 with a small ($\sim 10^{-5}$) volume fraction of sub-micron-sized glycol/water droplets. A horizontal section of the flow is illuminated by a light sheet produced by a combination of a customized, burst-mode Nd:YAG laser and a commercial pulsed laser. Three CCD cameras are employed in visualization. The "dynamic imaging camera" images the entire test section, but does not detect the individual droplets. It produces a sequence of instantaneous images of local droplet concentration, which in the post-shock flow is proportional to density. The gas curtain is convected out of the test section about 1 ms after the shock passes through the curtain. A second camera images the initial conditions with high resolution, since the initial conditions vary from test to test. The third camera, "PIV camera," has a spatial resolution sufficient to detect the individual droplets in the light sheet. Images from this camera are interrogated using Particle Image Velocimetry (PIV) to recover instantaneous snapshots of the velocity field in a small (19×14 mm) field of view. The fidelity of the flow-seeding technique for density-field acquisition and the reliability of the PIV technique are both quantified in this paper. In combination with wide-field density data, PIV measurements give us additional physical insight into the evolution of the Richtmyer-Meshkov instability in a problem which serves as an excellent test case for general transition-to-turbulence studies.

Received: 26 June 1999/Accepted: 29 October 1999

K. Prestridge, P. M. Rightley, P. Vorobieff[1], R. F. Benjamin, N. A. Kurnit
Dynamic Experimentation Division,
Los Alamos National Laboratory
MS P940, Los Alamos, NM 87545, USA

Present address:
[1]Department of Mechanical Engineering,
University of New Mexico, Albuquerque, NM 87131, USA

This work was supported by DOE contract W-7405-ENG-36.

1 Shock-tube facility

The experimental apparatus is a 5.5 m long horizontal shock tube with a 75 mm square cross-section (Budzinski et al. 1994; Jacobs et al. 1993, 1995; Rightley et al. 1997, 1999; Vorobieff et al. 1998). A membrane of thin polypropylene sheets separates the driver section, which is pressurized to 140 kPa, from the driven section. A laminar curtain of SF_6 gas flows downward across the test section at a velocity less than 10 cm/s and is drawn out the bottom of the test section (see Fig. 1). The flow is seeded with glycol/water droplets by forcing the SF_6 through the heating chamber of a modified theatrical fog generator along with the glycol/water mixture. The resulting mixture of SF_6 and glycol/water (fog) droplets then passes through a heat exchanger system, which condenses any remaining vapor, ensuring that the mixture which enters the test section is cool and incondensable. The addition of fog to the gas curtain was necessitated by the unavailability of multiple-pulsed lasers with enough energy-per-pulse to visualize the flow. Also, the fog droplets allow us to implement the PIV technique and the density-field visualization simultaneously. The gas curtain enters the test section through a varicose-patterned nozzle which imposes a perturbation upon the curtain cross-section. The nozzles can be changed to produce single- or multiple-wavelength initial perturbations (Rightley et al. 1999).

Three Hadland BR single-frame, intensified CCD cameras (effective resolution of 1134×468 pixels) image various regions within the test section. The cameras are operated using a PC with Hadland software, and the 3 images per event (one per camera) are stored on a Hadland frame-grabbing system and then transferred to a disk drive. The test section, pictured in Fig. 1, shows the orientation of the nozzle and the three cameras, and their approximate fields of view. The BRs are CCD cameras with 40-mm diameter Generation II intensifiers (MCP) with resolutions of 30 line pairs per mm. The intensifier is optically lens-coupled to the 8.8×6.6 mm CCD chip. A Nikon 105 mm lens at f:2.5 is used on the dynamic imaging camera, a Nikon 50 mm lens at f:5.6 is used on the initial conditions camera, and a Tamron Macro 1:1 90 mm at f:2.8 is used on the PIV camera. The cameras store one (IC camera), two (PIV camera), or six (dynamic imaging camera) images on their single frames, using the convection velocity to separate the images.

A doubled Nd:YAG laser (hereafter referred to as Laser A) was configured from existing components to emit up to

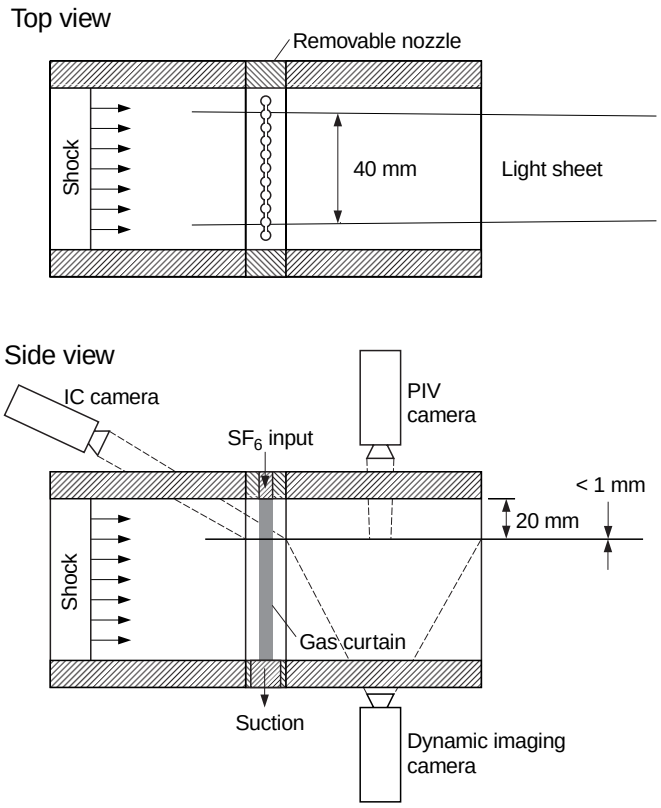

Fig. 1. Schematic of the shock tube test section showing position of light sheet and three CCD cameras

nine arbitrarily-spaced pulses within a 1 ms burst. This laser system consisted of a cw-pumped oscillator that could be acousto-optically Q-switched at arbitrary pulse spacing down to approximately 20 μs, followed by a series of four amplifiers that were double-passed by means of a Faraday rotator. A second Faraday rotator was used to provide additional feedback isolation. The amplifiers were staggered in time so that each could provide the gain needed for amplification of primarily two of the pulses in the train (one on the rising edge and one on the trailing edge of each 250 μs gain curve), and the amplifier timing and energy deposition could be varied to achieve the desired pulse balance. Individual pulses of up to 10 mJ in the green could be obtained by doubling 40 mJ of 1064 nm light in a KTP crystal, but this was close to the damage limit. Typically, the system was run with the 532-nm pulse energies varying from approximately 3 mJ to 5 mJ from the front to the back of the train to account for the decrease in particle density for the downstream images.

In some early experiments, the first amplifier was used to amplify three non-equally spaced pulses by using the fact that the first pulse from the oscillator had a substantially larger amplitude than the second, which was placed near the peak of the amplifier gain. The third pulse had an intermediate amplitude and could be amplified to be comparable to or larger than the others by careful adjustment of the amplifier timing. Some PIV measurements were initially made by decreasing the spacing between two of the later pulses in the train to 20 μs. However, it was difficult to obtain sufficient energy in the second of these pulses, and we have found that shorter time separations, down to 10 μs, were desirable for PIV interrogations. See Sect. 3 for a more detailed explanation of the determination of the optimal inter-pulse time. To satisfy these requirements, a second doubled Nd:YAG laser (Laser B), a New Wave Minilase 20-532NM, was added to the apparatus so that a single pulse from Laser B could be added to the light sheet in the test section at any time during the pulse train of Laser A. Each beam was allowed to expand over a long distance from a spherical focus to achieve the desired spanwise width of the light sheet (≈40 mm) so that it does not vary appreciably within the test section, as indicated in Fig. 1. In the vertical dimension, long, cylindrical focal length lenses are used to reimage and magnify the focus of the 532-nm beams to an approximately 1 mm width so that the sheet thickness does not vary appreciably over the test section, which is much shorter than the Rayleigh range of the beams. The beams are combined by passing one near the edge of a square mirror from which the other is reflected and directing them so that they overlap in the region of interest in the test section, which is located at a distance 20 mm below the nozzle (see Fig. 1). This positioning allows us to examine the gas curtain in a region that has been minimally affected by the disturbances from the suction outlet. A fast photodiode looking at reflected light allows the pulse amplitudes and inter-pulse time to be recorded on an oscilloscope to account for temporal or energy fluctuations. Laser A has a much longer pulsewidth (≈300 ns) than Laser B (≈10 ns) because of the lower gain of the cw-pumped oscillator, but is still sufficiently short that motion of the flow during the laser pulse is not significant.

The approximate fields of view of the three cameras are denoted in Fig. 1 with dotted lines. The IC camera focuses only on the initial conditions, in order to provide the best resolution possible for use in validation of numerical simulations. The PIV camera focuses on a small region of the flow, 19 mm streamwise × 14 mm spanwise. The location of the PIV camera is moved according to the placement of the PIV pulse from Laser B, and the PIV camera captures the closely-spaced pulses from both lasers. Since all of the cameras are single-frame, the PIV camera captures two exposures on one frame. The dynamic imaging camera focuses on the rest of the test section and captures the multiple pulses from Laser A only. This camera's intensifier is used as a shutter to block the single pulse from Laser B.

A solenoid plunger bursts the polypropylene diaphragm and sends a Mach 1.2 normal shock down the tube. The test section is ≈45 tube-widths downstream to enable the shock wave to become planar and stabilize before reaching the test section. The lasers and cameras are triggered by the passage of the shock past a pressure transducer mounted flush with the wall just upstream of the test section.

2 Diagnostics and data processing

The laser diagnostic system in our earlier shock-tube experiments was applied to acquire a series of instantaneous images of the density field (Rightley et al. 1997, 1999) with

tracer fidelity analysis carried out to verify that the water/glycol droplets do indeed follow the SF_6 in the gas curtain. The wide-field images from the dynamic imaging camera (Fig. 1) are similar to those acquired in these earlier studies, with a pixel resolution of about 0.1 mm – insufficient to detect the individual tracer particles, yet adequate to infer the local density from the intensity of light scattered off the multiple tracers within each pixel. In the 19×14 mm narrow-field window imaged by the PIV camera (Fig. 1), individual tracer particles can be detected, making it possible to apply the PIV diagnostics to double-exposed, highly-magnified flow images. Visual examination of the high-resolution PIV images reveals fine-scale structure which would be absent if the motion of the particles was dominated by inertia and if they were unable to follow the flow. We will present more quantitative evidence to validate this observation.

Seeding the flow field with particles which track the flow reliably is crucial for the success of the PIV technique. Refer to Adrian (1991) for a review of PIV diagnostics and to Melling (1997) for a summary of the issues involving the use of particles in PIV. The introduction of the PIV diagnostic prompts us to reexamine the issue of the flow-tracking fidelity. Below we reproduce some of our earlier results for previous gas curtain experiments where PIV was not implemented (Rightley et al. 1999), and present new, PIV-specific data, outlining several approaches to estimating the flow tracking fidelity of the glycol/water droplets.

The average diameter of the droplets produced by the fog generator/heat exchanger combination is ≈0.5 μm (Entertainment Services and Technology Associates 1996). What must be determined first is how well these droplets can follow the strong acceleration of the shock wave, and here we follow the approach described by Hjelmfelt and Mockros (1966). They studied the terms which affect the way higher density particles in a lower density carrier phase respond to velocity fluctuations of the carrier phase. Using their analysis, we can estimate the largest particle sizes which will be able to follow the fluctuations of the carrier phase well enough for the purposes of PIV and imaging. The motions of the particles are dominated by a balance between Stokes' drag and inertia. For particles much denser than the carrier phase, buoyancy, added mass and the dynamic pressure field can all be neglected (Hinze 1959). For this size of particle, the Weber number, *We*, is small, where

$$We = \frac{d_p \rho_g U^2}{\sigma} = \frac{\text{inertial forces}}{\text{surface tension}} \quad , \tag{1}$$

and d_p is the particle diameter, ρ_g is the density of the carrier phase, and U is a characteristic relative velocity. Using values for the droplets in the gas curtain, the Weber number is in the approximate range, $0.001 \leq We \leq 0.1$, during the entire event. Such small Weber numbers mean that the particles can be considered spherical, except possibly for a short time during the shock compression phase. We are interested in whether or not the particle fluctuations can follow the gas fluctuations, and Hjelmfelt and Mockros estimated this by rewriting the velocities of the particles, v_p, and gas, v_g, in frequency space, such that:

$$\overrightarrow{v_p}(\omega) = \int_{-\infty}^{\infty} \overrightarrow{u_p}(\tau) e^{-i\omega\tau} d\tau \tag{2}$$

and

$$\overrightarrow{v_g}(\omega) = \int_{-\infty}^{\infty} \overrightarrow{u_g}(\tau) e^{-i\omega\tau} d\tau \quad . \tag{3}$$

This formulation introduces a characteristic frequency of the flow, ω. Using the force balance (inertia = Stokes' drag), we can write the ratio of the fluctuations in the form (Hjelmfelt and Mockros 1966):

$$\frac{|\overrightarrow{u_p}|^2}{|\overrightarrow{u_g}|^2} = \frac{v_p v_p{}^*}{v_g v_g{}^*} = \frac{(18St^2/s)^2}{(18St^2/s)^2 + 1} \quad , \tag{4}$$

where

$$St = \sqrt{\frac{\nu_g}{\omega d^2}} \text{ is a Stokes' number and } s = \frac{\rho_p}{\rho_g} \tag{5}$$

and the * indicates the complex conjugate. The Stokes drag model is used here in order to simplify the analysis, and because it provides sufficient accuracy (to within 15%) based on a conservative particle Reynolds number of 1. Also, the Stokes drag underpredicts the drag coefficient at higher Reynolds numbers, which results in a more conservative estimate of the frequencies a particle can follow.

We require that the energy spectrum of the fluctuations of the particles be within 1% of the spectrum of the fluctuations of the gas. This applies a very strong constraint on the limit of acceptable particle diameters. For an estimate of the early-time frequencies to which the particles are subjected, let us consider the width of the gas curtain and the shock speed. A characteristic frequency of the flow constructed from a shock speed of 400 m/s and a 6 mm curtain width is $\omega = 400/0.006 = 67$ kHz. This frequency can be followed by particles which are at most 0.6 μm in diameter. At late times, there are several ways to estimate the flow frequencies. One could use the PIV grid spatial resolution, which is 0.5 mm, and the approximate maximum fluctuating velocity component, where the fluctuating velocity, $\mathbf{v}'$, is defined as

$$\mathbf{v}'(\mathbf{t}) = \mathbf{v}(\mathbf{t}) - \bar{\mathbf{v}}(\mathbf{t})_{\text{convective}} \quad , \tag{6}$$

where $\mathbf{v}$ is the local velocity and $\bar{\mathbf{v}}_{\text{convective}}$ is the mean convective velocity of the flow. Typically, $\mathbf{v}'/\bar{\mathbf{v}}_{\text{convective}} < 0.1$. Then an estimate of the frequency, based upon a fluctuating velocity of 10 m/s would be only 20 kHz, and the particles need only be less than 1.1 μm. For a more conservative estimate, the smallest time separation between PIV images must be set to 10 μs, corresponding to a frequency of 100 kHz. This inter-pulse time is determined by the convection velocity of the curtain, magnification of the PIV imaging region, and the pixel resolution of the camera. More details about how the inter-pulse time was determined are included in the next section. This timing requires that the particles be at most 0.5 μm in diameter. Even at this most stringent requirement, the fog droplets (0.5 μm diameter) are still able to

follow 99% of the velocity fluctuations. The analysis above is in some ways analogous to the estimation of the turbulent *rms* error as described by Adrian (1995). We cannot apply the estimation procedure described in this paper directly because at present we do not have the velocity statistics necessary to estimate the Taylor microscale, λ_T.

For an alternative, direct check of the droplet tracking fidelity, we can compare the images of direct Rayleigh scattering (RS) of SF_6 from earlier experiments (Budzinski et al. 1994) to images of light scattered from the fog droplets. Figure 2 (top) shows an image from the experiments of Budzinski et al. (1994). The image is formed by the direct Rayleigh scattering of the SF_6 in the gas curtain using a powerful laser sheet. The images are of the initial conditions and a single dynamic image at $t = 450$ μs. We compare this image with a recent shot, which uses glycol/water droplets to seed the SF_6 curtain to increase the light scattering efficiency. The lower image in Fig. 2 is an image of light scattering by the fog using the current pulsed light sheet. The similarity of the images strongly suggests that the fog particles track the SF_6 reliably.

A more detailed examination can be made by looking at the intensity profiles through cross-cuts of similar flow features. Figure 2 shows white lines where the intensity profiles were sampled. No smoothing of the data was done. Figure 3 plots the profiles of pixel intensity through the initial and dynamic conditions. All of the pixel intensities are normalized with peak-intensity values, and the spatial distance is normalized with the wavelength of the initial perturbation. The comparison between the initial conditions is excellent. The initial conditions also show the diffuse nature of the curtain's upstream and downstream interfaces, and the fact that there seems to be no difference between the diffusivity of the SF_6 in the curtain and the fog droplets. At the later time, the comparison was made between the most symmetric mushroom structures. Again, the evidence indicates that the glycol droplets are following the SF_6. The dip in intensity of the fog sample at $x/\lambda = 0.6$ is caused by the increased spatial resolution of the fog images, causing enhanced contrast within the mushroom. From this direct evidence, we are confident that accurate wide-field density and narrow-field velocity information can be ascertained through the use of the fog as a tracer.

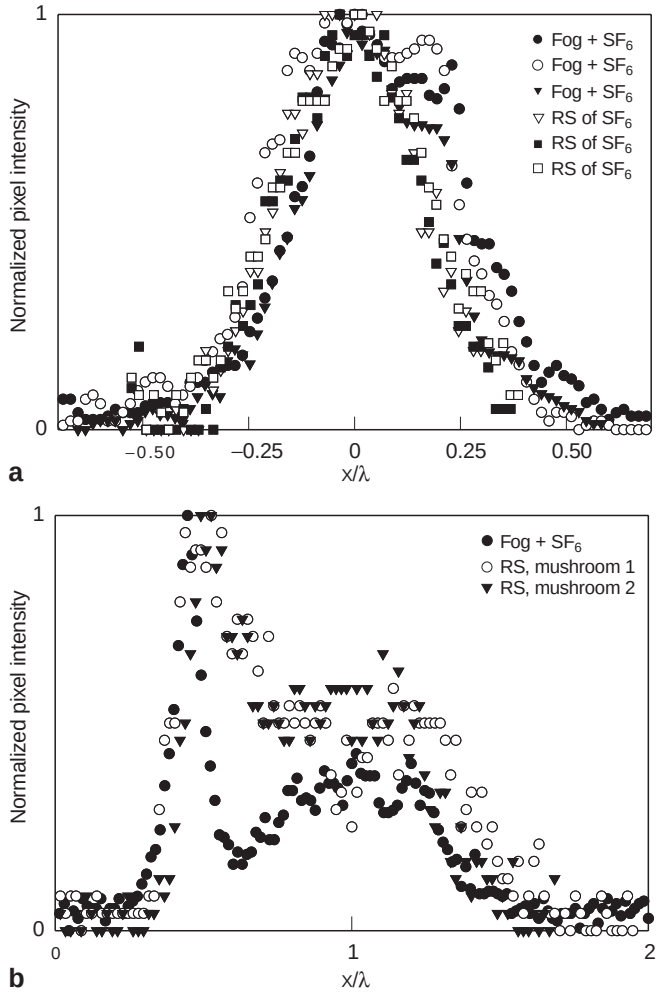

Fig. 3a, b. Comparison of normalized pixel intensities for initial conditions **a** and downstream **b**. Samples are taken from labelled lines in Fig. 2

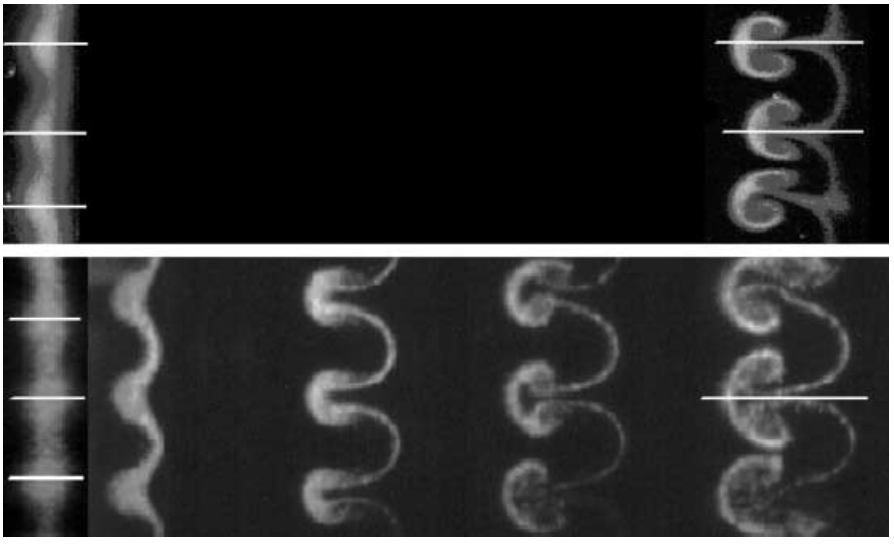

Fig. 2. Direct Rayleigh scattering from SF_6 at $t = 0$ and 450 μs (*top*), from Budzinski et al. (1994), and scattering from fog and SF_6 at $t = 0$, 60, 200, 340 and 480 μs (*bottom*). White lines indicate where pixel intensity samples were taken

Finally, one must account for the PIV interrogation error due to the limited optical resolution of the system. Sub-pixel resolution cannot be achieved with our setup, because the tracer particle size is considerably smaller than the size of the area imaged in one pixel. Thus the accuracy in reconstructing the velocity field is limited by the pixel resolution and time interval between the exposures, leading to an error up to 0.75% for the 10 μs interexposure delay.

3 Observations

The following observations represent a small sample of the data which has been collected so far, and they are intended to serve as an illustration of the capabilities of the diagnostics as well as the accuracy of the implementation of PIV. The feasibility of the PIV technique was demonstrated earlier on the gas-curtain experiment using a double-pulsed Nd:YAG laser and a 512 × 512-pixel CCD camera (Vorobieff et al. 1997). One of the primary reasons for implementing PIV in this experiment is to improve the quality of information available for validation of numerical simulations. With this goal in mind, we will provide an example of the qualitative and quantitative information which can be obtained from velocity fields. The ultimate goals will be a detailed phenomenological understanding of transition to turbulence, to provide much more extensive statistical information for code validation efforts and to improve physics models.

Figure 4a and b are two examples of initial conditions and dynamic images of the density field which are captured in each experimental event. The spatial resolution of the dynamic images is 0.1 mm/pixel. In these shots, the single-mode nozzle (one wavelength, $\lambda = 6$ mm, one amplitude) was used, and these images were selected due to their similar dynamic evolutions. The initial conditions of the experiment vary slightly from shot to shot due to fluctuations in the flow through the nozzle. For some shots, this changes the conditions from single-mode to more complex initial conditions, accelerating a transition to turbulence which becomes apparent within the length of the test section. In both of these shots, however, the gross features and evolution of the flow are similar, including the stretched mushrooms caused by slightly lower amplitude perturbations in one location along the initial conditions. These images also appear similar in terms of the integral estimate of the mixing region growth.

Through the use of quantitative measures, we would like to be able to compare these two shots and determine what similarities and differences they possess beyond those apparent through visual inspection. It is for this purpose that the PIV camera is focused on a small region of the gas curtain. Figure 5a and b show the images from the PIV camera of the two regions outlined by white boxes from Fig. 4a and b. Note that in these images, the spatial resolution is 15 μm/pixel, in contrast to the 100 μm/pixel of the dynamic images. The figures show the two laser pulses which illuminate the flow, with a time

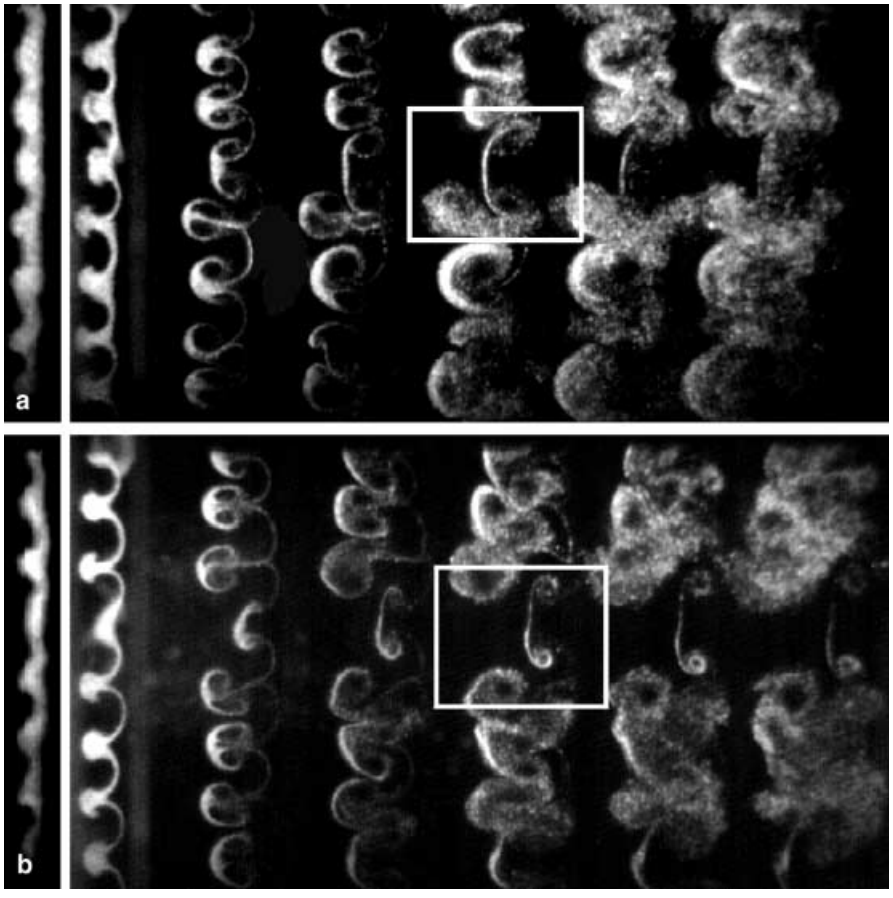

Fig. 4a, b. Case 1 **a** and Case 2 **b**. Initial ($t = 0$) and dynamic ($t = 50$, 190, 330, 470, 610, 750 μs) conditions for single mode nozzle, as viewed by the IC and Dynamic cameras. White box indicates field of view of PIV camera

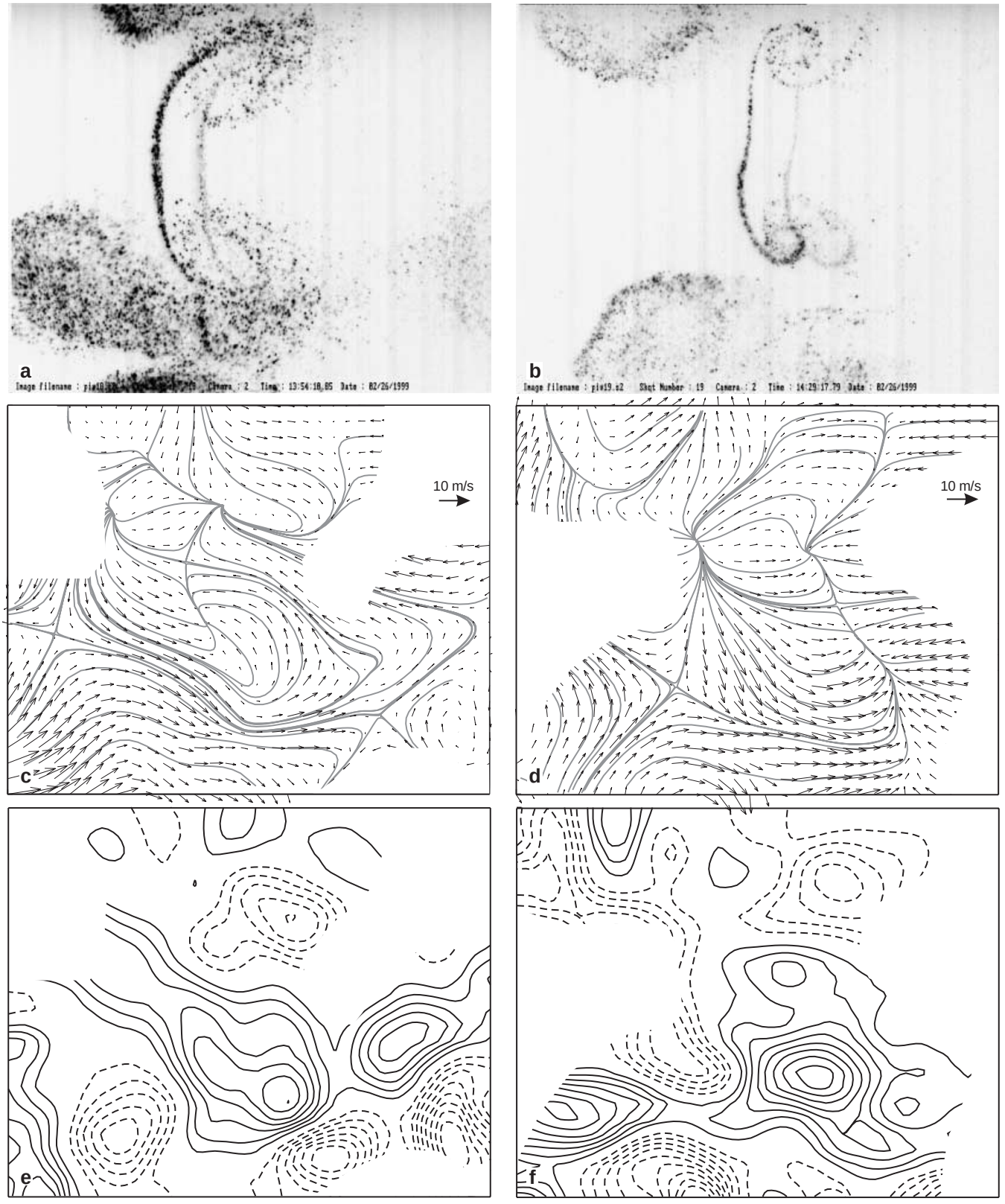

Fig. 5a–f. PIV analysis. Case 1 **a** and Case 2 **b**, both captured using the PIV camera. Negative images are shown, with dark regions corresponding to high scattering intensity from fog droplets. Velocity fields for Case 1 **c** and Case 2 **d** are shown in the second row. The mean velocity (97 m/s in both cases) has been subtracted and instantaneous streamlines are shown. Vectors from regions missing particle pairs have been removed. Vorticity fields for Case 1 **e** and Case 2 **f** are shown in the last row. Positive (solid) and negative (dashed) contours at vorticity values of ±1000, ±2000,…,±8000 s^{-1} are shown

separation of 10.4 μs. The time separation between PIV pulses (pulse from Laser B and nearest pulse from Laser A) was optimized, weighing the need to accurately determine both the mean convective velocity of the curtain ($\bar{\mathbf{v}}_{\mathbf{convective}} \approx 100$m/s) and the fluctuating velocity ($\mathbf{v}' \approx 10$ m/s), as defined by Eq. (6). 10 m/s is the typical maximum measured value for the fluctuation velocity. The time separation was selected to be large enough to resolve (over at least five pixels) the fluctuation velocities, but small enough to minimize the loss in spatial resolution caused by the particles traveling quickly downstream between pulses. Optimally, this inter-pulse time for PIV was 10 μs ≤ Δt < 20 μs based on a spatial resolution of ≈15 μm/pixel for the PIV camera. This resolution and inter-pulse time results in an error of less than 0.3% in the mean convective velocity measurement.

The two images in Fig. 5a and b were interrogated using VISIFLOW PIV analysis software (AEA Technology 1997). Due to the particle distribution at this time in the flow evolution, interrogation box sizes of 64 pixels square were used to search for particle pairs. A technique of single frame cross-correlation was used (AEA Technology 1997), and the second box was displaced downstream from the first using an estimated freestream velocity of 100 m/s. The resulting fluctuating velocity fields are shown in Fig. 5c and d, along with instantaneous flow streamlines.

In Fig. 5c and d, the velocity fields have many features in common. In both cases, the mean velocity is 97 m/s, and it has been subtracted in order to show the fluctuating components of velocity. The velocity vectors have been smoothed using a Gaussian 5 × 5 filter to reduce noise. An edge-detection algorithm was applied to the images to determine regions without apparent particle pairs. The information from these regions is blanked out in the velocity and vorticity plots and not used in the histogram analysis presented later in this paper. The instantaneous velocity fields for each case are also very similar. They show good correspondence with the visible large-scale features of the images, including the roll-up of fluid behind the elongated mushrooms. Also visible are the nearby mushroom structures at the top and bottom edges of the pictures, which induce strong localized effects on the velocity field. The locations of these features are different in each case. The streamlines oriented vertically show the positions of the elongated mushrooms, which are similar in size and location in each event. Note that the stagnation points (indicated by ×-shaped streamlines) upstream of both mushrooms are in different locations, emphasizing the slightly different dynamics of the vortex structures surrounding the elongated mushrooms.

Evidence of a mixing transition has been seen in the second-order structure function analysis of pixel intensity (Vorobieff et al. 1998), histogram analysis of the dynamic images (Rightley et al. 1999), and fractal dimension of level sets of pixel intensity (Vorobieff et al. 1999). At late times (> 500 μs), a mixing transition is apparent in the curtain. Because the PIV is analyzed at a late time in the flow (≈470 μs), we know that this is close to when mixing transition has been observed to occur (Rightley et al. 1999; Vorobieff et al. 1998, 1999). Figure 6 shows a distribution of the magnitudes of velocity of vectors from

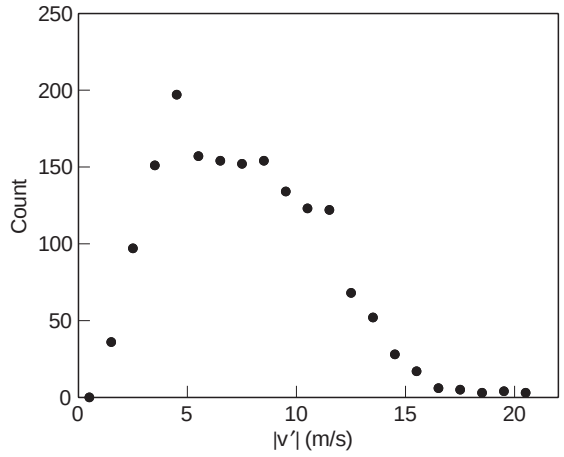

Fig. 6. Histogram of fluctuation-velocity magnitudes

Fig. 5c and d. As can be seen in the figure, most of the magnitudes lie between 4 and 9 m/s. Based on this velocity range, the Reynolds number of the flow is $10000 < Re < 22500$, where $\nu_{SF_6} = \nu_{\mathrm{air}}/6 = 2.4 \times 10^{-6}$ m^2/s, and $L = \lambda = 6$ mm. Thus the mixing transition Reynolds number can be expected to lie within the above range.

The velocity histogram, Fig. 7, shows the distributions of the streamwise, v'_x, and spanwise, v'_y fluctuating velocity components for Fig. 5c and d. The open circles correspond to the streamwise component of velocity, and the closed circles correspond to the spanwise component. Based on the dynamic visualization of the curtain, we know that the flow is anisotropic, and variations in the two distributions show that the spanwise velocity fluctuations have a wider distribution of magnitudes than the streamwise fluctuations. More information can be determined from these velocity fields by calculating vorticity and other derivative quantities. The velocity fields in Fig. 5c and d have been smoothed using a Gaussian filter, as mentioned previously.

Figure 5e and f show the ω_z component of vorticity calculated from Fig. 5c and d, with solid lines indicating positive vorticity and dashed lines indicating negative

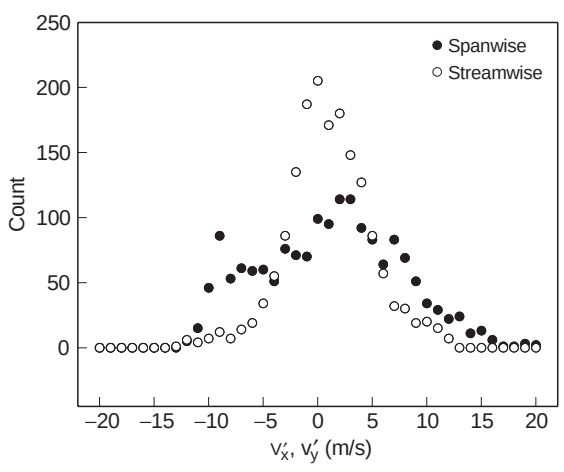

Fig. 7. Histogram of streamwise (○) and spanwise (•) fluctuating velocities

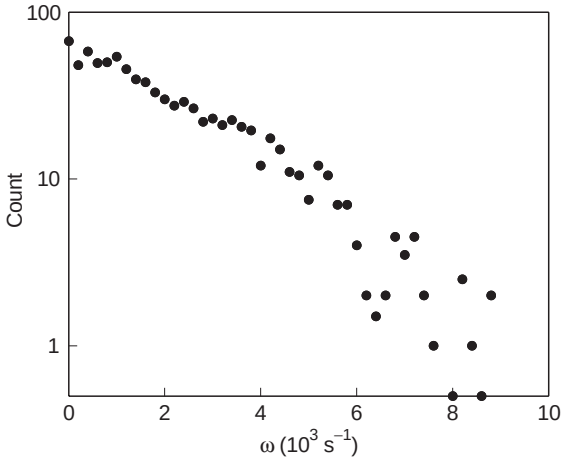

Fig. 8. Histogram of out-of-plane vorticity magnitude, log-linear scaling

vorticity. We can confirm the large-scale coherent vortex structures in both cases. For each case, the positive and negative vortices behind the elongated mushrooms are visible and of similar magnitudes. Also visible are the vortex structures with negative vorticity in the lower part of each figure. What these images help to highlight are the different relative positions of the vortex patches in the two different shots. Although the vortices of the elongated mushroom structures are in similar positions, the surrounding vortices are positioned differently. In Case 1, Fig. 5e shows a negative vortex almost directly upstream of the positive vortex patch from the elongated mushroom. Figure 5f shows that the negative vortex is still laterally displaced from the positive end of the elongated structure, although it is also upstream of that structure. Therefore, the velocity and vorticity fields show additional differences in the flow which could not be identified from the dynamic density-field images of Fig. 4a and b.

A histogram of the vorticity magnitude distributions from Fig. 5e and f is shown in Fig. 8. The high-magnitude vorticity corresponds to the vortex cores, which are associated with the large-scale, coherent mushroom structures in the flow. This general shape of the vorticity distribution has been reproduced over many shots. These vorticity histogram data are consistent with what one would expect from a vortex-dominated, possibly turbulent flow.

4 Conclusions

We have demonstrated an application of PIV to the study of the Richtmyer-Meshkov instability. This technique, although not new in the fluids community, has not been previously used to study the high-speed evolution of a shock-accelerated instability. The important issue of fog particle tracking fidelity has been reviewed in light of the concerns posed by the use of PIV, and we are confident that the fog droplets are following the velocity fluctuations of the SF_6 density field at both early and late times. We have shown that the information available from PIV allows us to resolve features of the flow field which are smaller than the initial perturbations of the gas curtain. Velocity fields reveal differences in the flow features which are not apparent in density-field visualizations. The positions of vortex cores cannot be ascertained from the density field visualizations, yet their magnitudes and positions are available from the velocity fields, and the interactions between neighboring cores can be more readily surmised. This quantitative information now available enables us to determine quantitative differences in events which may have similar appearances based on density-field visualizations alone.

References

Adrian RJ (1991) Particle-imaging techniques for experimental fluid mechanics. Ann Rev Fluid Mech 23: 261

Adrian RJ (1995) Limiting resolution of particle image velocimetry for turbulent flow. Adv Turb Research-1995: 1

AEA Technology (1997) VISIFLOW System User Manual. Oxfordshire, UK

Budzinski JM; Benjamin RF; Jacobs JW (1994) Influence of initial conditions on the flow patterns of a shock-accelerated thin fluid layer. Phys Fluids 6: 3510

Entertainment Services and Technology Associates (1996) Introduction to modern atmospheric effects. New York

Hinze JO (1959) Turbulence. New York: McGraw-Hill

Hjelmfelt AT; Mockros LF (1966) Motion of discrete particles in a turbulent fluid. Appl Sci Res 16: 149

Jacobs JW; Klein DL; Jenkins DG; Benjamin RF (1993) Instability growth patterns of a shock-accelerated thin fluid layer. Phys Rev Lett 70: 583

Jacobs JW; Jenkins DG; Klein DL; Benjamin RF (1995) Nonlinear growth of the shock-accelerated instability of a thin fluid layer. J Fluid Mech 295: 23

Melling A (1997) Tracer particles and seeding for particle image velocimetry. Meas Sci Tech 8: 1406

Meshkov EE (1969) Instability of the interface of two gases accelerated by a shock wave. Izv Akad Nauk SSSR Mekh Zhidk Gaza 4: 151

Richtmyer RD (1960) Taylor instability in shock acceleration of compressible fluids. Commun Pure Appl Math 23: 297

Rightley PM; Vorobieff P; Benjamin RF (1997) Evolution of a shock-accelerated thin fluid layer. Phys Fluids 9: 1770

Rightley PM; Vorobieff P; Martin R; Benjamin RF (1999) Experimental observations of the mixing transition in a shock-accelerated gas curtain. Phys Fluids 11(1): 186

Vorobieff P; Rightley PM; Benjamin RF (1997) Mushrooms with a smile: Richtmyer-Meshkov growth of multiwavelength perturbations. Gallery of Fluid Motion, APS-DFD Meeting, Nov. 23–25, San Francisco CA

Vorobieff P; Rightley PM; Benjamin RF (1998) Power law spectra of incipient gas curtain turbulence. Phys Rev Lett 81(11): 2240

Vorobieff P; Rightley PM; Benjamin RF (1999) Shock driven gas curtain: fractal dimension evolution in transition to turbulence. Physica D 133: 469